Nonlinear Dynamics (2026) 114:616
https://doi.org/10.1007/s11071-025-12176-y

RESEARCH

Mitigation of vortex-induced vibrations in transmission lines via a nonlinear moving absorber

Ehab Basta[1] · **Sunit K. Gupta**[1] · **Oumar R. Barry**[1]

Received: 1 August 2025 / Revised: 30 November 2025 / Accepted: 22 December 2025

Abstract

Aeolian vibrations are a major contributor to fatigue in overhead power transmission lines. These oscillations are commonly controlled using fixed dampers, such as Stockbridge units. Nevertheless, the performance of such dampers strongly depends on proper tuning and placement along the line, which can limit their effectiveness under varying operational conditions. To overcome these limitations, moving vibration absorbers have been proposed as a more adaptable solution. However, despite their promise, existing literature has largely neglected the nonlinear effects introduced by both the wind-induced lift force and the dynamic behavior of the moving vibration absorbers themselves. While prior work has studied either fixed nonlinear absorbers or mobile linear absorbers under wind-induced vibrations, this study, for the first time, combines a nonlinear wind excitation model with four nonlinear dynamic absorber profiles, including two two-way motion profiles, and quantifies vibration suppression under transient wind conditions. The aerodynamic lift due to wind is represented using a nonlinear Van der Pol oscillator, whereas the vibration absorber exhibits a restoring force with a cubic stiffness component. Through numerical simulations, we evaluate the performance of nonlinear vibration absorbers with different motion profiles under resonance conditions. Results indicate that nonlinear moving vibration absorbers are more effective in suppressing transverse vibrations compared to their linear, fixed counterparts, offering a more robust damping mechanism. Furthermore, parametric studies explore the effects of absorber velocity, nonlinear stiffness, and damping ratio on system response. We find that the two two-way motion profile consistently yields the highest energy dissipation efficient, hence, superior vibration suppression. These findings offer new guidelines for the design of advanced damping systems in power transmission lines subjected to wind-induced vibrations.

Keywords Self-excited oscillator · Nonlinear moving absorber · Powerline · Vortex-induced vibration · Aeolian vibration · Structural vibration mitigation

1 Introduction

Wind-induced (Aeolian) vibrations in high-voltage power lines represent a critical phenomenon that significantly impacts the structural integrity and reliability of these systems. These vibrations are typically characterized by small amplitude flexural oscillations caused by the interaction between light to moderate-speed winds with the conductor's natural frequency [1]. Despite their small amplitude, these vibrations can lead to fatigue and ultimately, the failure of the transmission lines, potentially resulting in catastrophic damages to the cables [2, 3]. Therefore, the development of effective vibration mitigation strategies for transmission lines during aeolian vibrations has become a critical area of research.

Traditionally, passive dampers, such as Stockbridge dampers, are employed to control undesirable vibrations in power transmission lines [4–7]. The popularity of passive dampers is attributed to their cost-effectiveness, simplicity, reliability, and ease of maintenance. Their effectiveness has been demonstrated across a wide range of wind- and flow-induced vibration problems, including cable vibration control, passive mitigation of aeroelastic instabilities, and suppression of flutter and limit-cycle oscillations in lifting surfaces. By dissipating or redirecting vibration energy, these devices reduce oscillation amplitudes and enhance the stability of engineering systems under wind-induced conditions.[8–10]. Within

✉ Oumar R. Barry
obarry@vt.edu

[1] Department of Mechanical Engineering, Virginia Tech, Blacksburg, VA 24061, USA

Published online: 28 April 2026

power transmission lines specifically, the performance of a Stockbridge damper depends on the number of resonant frequencies it can achieve and its placement along the span of the conductor [11–13]. Typically, these dampers are installed near the ends of the conductor, primarily due to the improved accessibility in these regions, which facilitates inspection and simplifies maintenance procedures. However, in these locations, variable wind patterns can diminish the overall performance of the dampers due to variations in the amplitude and frequency of the wind. For instance, the fixed position of a Stockbridge damper may coincide with nodal points of a vibration mode of the conductor, significantly hindering its ability to mitigate vibration [11].

To address the challenges associated with fixed Stockbridge dampers, Bukhari et al. [14] investigated the use of moving vibration absorbers on power lines. Later, Kakou et al. [11] implemented a PID-based control system on a moving absorber for both vibration suppression and power line inspection. Both studies suggest that moving absorbers outperform their fixed counterparts in vibration suppression. However, these studies have not yet considered the effects of nonlinearity in fluid–structure interaction and the behavior of moving absorbers.

While aeolian vibrations are similar to vortex-induced vibrations (VIV), they are distinct in their manifestation. Aeolian vibrations occur due to the cross-flow of air over slender bodies, such as powerlines, and are typically associated with higher frequency and low amplitude [15]. In aeolian vibrations, the unsteady aerodynamic force caused by the cross-flow of wind over power lines forms a boundary layer that separates near the rear end of the cross-section of the body. As the flow passes the structure, vortices are shed, forming a von Karman vortex street in its wake. This alternating shedding generates an uneven pressure distribution along the structure, producing fluid forces that can excite the structure's natural frequencies and induce aeolian vibrations. [16]. Due to the complex nature of these interactions, sinusoidal force approximations are often inadequate for moving bodies such as stretching cylinders and sheets [17–19]. Consequently, more sophisticated models for the wake-oscillator, such as the van der Pol-type [20] or a Rayleigh type [21] oscillators, have been employed to more accurately represent these phenomena. These models, which integrate self-sustaining oscillations via mechanisms such as negative damping, provide a more accurate representation of the complex dynamics involved in VIV and Aeolian vibrations. Empirical validations of these models have shown good agreement with experimental observations, establishing them as valuable tools for understanding and predicting the dynamics of structures subjected to VIV [22–24].

To handle the nonlinear WIV caused by the nonstationary and stochastic nature of wind, which can be modeled as the nonlinear van der Pol oscillator [7, 25, 26], nonlinear vibration absorbers have been found to be more effective [27–32]. Recent investigations in other high-performance structures have demonstrated the effectiveness of nonlinear and adaptive vibration mitigation. These include nonlinear energy-sink–based (NES) spacecraft vibration control with integrated energy harvesting [33], active varying-stiffness NES designs that improve broadband suppression [34], and high-static–low-dynamic-stiffness isolators employing adjustable buckling beams for improved attenuation [35]. Collectively, these studies highlight the capability of nonlinear mechanisms to provide robust vibration attenuation. The superiority of nonlinear vibration absorbers over their linear alternatives can be attributed to their ability to suppress vibrations over a wide frequency spectrum [27, 29], and their robustness against unpredictable environmental conditions [30]. For example, Samani et al. [31] investigated the effect of a nonlinear tuned dynamic absorber versus a linear tuned dynamic absorber to control the vibration of a beam with a moving load. They observed that nonlinear vibration absorbers with cubic nonlinearity significantly reduced the maximum amplitude of vibrations. More recently, Zhang et al.[32] studied the vibration capability of a nonlinear energy sink with cubic nonlinear damping. They observed that a cubic nonlinear-damping NES could outperform its linear-damping NES counterpart in mitigating vibrations within nonlinear systems.

Although previous studies [11, 14] have demonstrated the superior performance of moving absorbers compared to fixed absorbers in suppressing vibrations, they have overlooked the combined nonlinearities present in both wind-structure interaction and absorber dynamics. This nonlinear interaction between the vibration absorber and the wind plays a critical role in determining absorber performance, especially under transient wind excitation. In this work, for the first time, we numerically investigate the combined effect of a nonlinear aerodynamic lift force, represented using a nonlinear wake oscillator, and a nonlinear moving vibration absorber with cubic stiffness and damping. Euler-Bernoulli beam is employed to model the conductor,while the nonlinear moving absorber is represented as a lumped-parameter spring-mass-damper system. Four different motion profiles for the absorber, including the novel two-two-way motion profile, are studied under resonance conditions. The performance of various configurations of the moving absorber is analyzed and compared to that of a fixed absorber through time-history analysis. We observe the superior performance of the two two-way moving nonlinear vibration absorber profiles in suppressing vibrations in overhead power transmission lines. Parametric studies are also conducted to evaluate the effects of system parameters, including absorber velocity, nonlinear stiffness, and mass ratio. Overall, this contribution represents a novel and comprehensive approach to modeling aeolian vibration suppression, where nonlinear

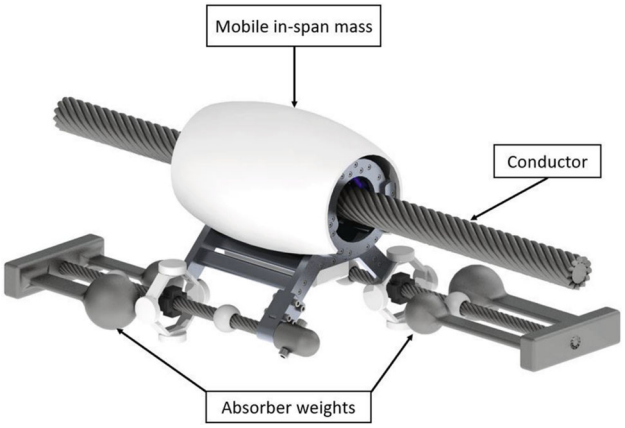

Fig. 1 Design concept of the moving absorber embedded to an overhead conductor [11]

excitation, nonlinear absorption, and dynamic mobility are jointly considered.

The rest of the paper is organized as follows. In Sect. 2, we present the mathematical model for the coupled system of beam–wake oscillator along with a discussion on model convergence. Section 3 examines the effectiveness of the nonlinear absorber in suppressing conductor vibrations. A detailed study on the influence of key parameters on the system response and an evaluation of the absorber's efficiency are also provided. Finally, conclusions are drawn in Sect. 4.

2 Mathematical modeling

A prototype of a moving vibration absorber for power lines, as proposed by Kakou et al. [11], is illustrated in Fig. 1. The design of this absorber is inspired by power line inspection robots and Aeolian vibration damper technology [36]. A schematic of the dynamic system, including a cable with a moving damper at different time-instants, is presented in Fig. 2. For the current analysis, the powerline is modeled as an Euler-Bernoulli beam with length l, flexural rigidity EI, mass per unit length m, and is subjected to an axial pretension force T. The moving absorber is modeled as an span-mounted mass-spring-damper-mass system, comprising an span-mounted mass m_c, vertically suspended mass m_{ab}, linear and nonlinear stiffness components k and k_{nl}, respectively, and linear and nonlinear viscous damping components c and c_{nl}, respectively.

The moving absorber traverses along the length of the conductor with a constant velocity of v_{ab}. Let x_c and x_{ab} denote the positions of the mass along the span and the vertically suspended absorber, respectively, along the conductor length $[0,\ l]$. We can express the velocity as

$$v_{ab} = \dot{x}_c = \dot{x}_{ab}.$$

Let $w(x,t)$ denote the transverse displacement of the cable at a point x, $w(x_c,t)$ the transverse displacement of the span-mounted mass at position x_c at a time t and $z(t)$ the transverse displacement of the absorber mass at a time t. Thus, the position vectors for a point in the cable at x, the span-mounted mass, and the absorber mass at a given time t are given by

$$\boldsymbol{r_{bm}} = x\boldsymbol{i} + w\,(x,t)\,\boldsymbol{j}, \tag{1a}$$
$$\boldsymbol{r_c} = x_c\,(t)\,\boldsymbol{i} + w\,(x_c,t)\,\boldsymbol{j}, \tag{1b}$$
$$\boldsymbol{r_{ab}} = x_c\,(t)\,\boldsymbol{i} + z\,(t)\,\boldsymbol{j}. \tag{1c}$$

Subsequently, the velocity vectors for a point x in the beam, the span-mounted mass, and the absorber mass are given by

$$\dot{\boldsymbol{r}}_{\boldsymbol{bm}} = \frac{\partial w\,(x,t)}{\partial t}\boldsymbol{j} \tag{2a}$$
$$\dot{\boldsymbol{r}}_{\boldsymbol{c}} = v_{ab}\boldsymbol{i} + \left(\left.\frac{\partial w}{\partial t}\right|_{x=x_c} + \left.\frac{\partial w}{\partial x}\right|_{x=x_c}\cdot v_{ab}\right)\boldsymbol{j} \tag{2b}$$
$$\dot{\boldsymbol{r}}_{\boldsymbol{ab}} = v_{ab}\boldsymbol{i} + \dot{z}\boldsymbol{j} \tag{2c}$$

Accordingly, the total kinetic energy of the system is given by

$$T = T_{bm} + T_c + T_{ab}\,, \tag{3}$$

where T_{bm}, T_c, and T_{ab} represent the kinetic energies of the beam, the span-mounted, and the absorber, respectively, and are given by:

$$T_{bm} = \frac{1}{2}\rho A\int_0^l \dot{w}^2\,dx\,, \tag{4a}$$
$$T_c = \frac{1}{2}m_c\int_0^l\left[v_{ab}^2 + \left(\dot{w} + w'v_{ab}\right)^2\right]\delta\,(x - x_c)\,dx\,, \tag{4b}$$
$$T_{ab} = \frac{1}{2}m_{ab}\left[v_{ab}^2 + \dot{z}^2\right]. \tag{4c}$$

In the above expressions, the Dirac delta function $\delta(x-x_c)$ is introduced to ensure that the kinetic energy of the span-mounted mass is evaluated at the position $x = x_c$, where the deflection of the span-mounted mass matches the transverse deflection of the cable.

Next, the system's stored potential energy, U, is given by

$$U = U_{bm} + U_{ab} + U_P, \tag{5}$$

where U_{bm} is the strain energy due to the flexural deformation of the beam, U_{ab} is the potential energy associated with the deformation of linear and nonlinear springs of the absorber, and U_P represents the work done by the axial tension due to the deformation of the cable. In the current

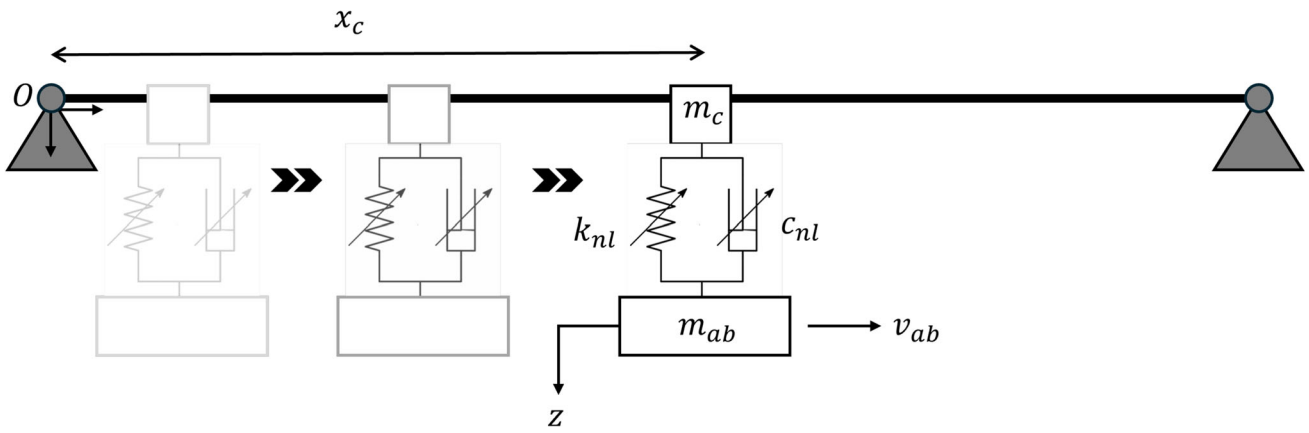

Fig. 2 Schematic of a nonlinear moving absorber on the overhead conductor

analysis, the conductor is supported at both ends. Additionally, the axial pretension P is kept constant throughout the analysis. Accordingly, these components are expressed as

$$U_{bm} = \frac{1}{2} EI \int_0^l \left(w''\right)^2 dx\,, \tag{6a}$$

$$U_{ab} = \int_0^l \left\{ \frac{1}{2} k \left(w - z\right)^2 + \frac{1}{4} k_{nl} (w - z)^4 \right\} \delta\left(x - x_c\right)\, dx\,, \tag{6b}$$

$$U_P = \frac{1}{2}\, P \int_0^l \left(w'\right)^2 dx\,. \tag{6c}$$

The work done by nonconservative forces, such as fluid–structure interaction and viscous dissipation through the damper, is given by [37]

$$W_T = \int_0^l f_w\, w dx + \left[\int_0^l \left\{ \frac{1}{2} c \left(\dot{w} + w' v_{ab} - \dot{z}\right)^2 + \frac{1}{4}\, c_{nl} \left(\dot{w} + w' v_{ab} - \dot{z}\right)^4 \right\} \delta\left(x - x_c\right)\, dx \right]. \tag{7}$$

In Eq. 7, the first integral represents the work done by the fluid–structure interaction, where $f_w w\, dx$ quantifies the energy input from the fluctuating lift force f_w acting over the transverse displacement w. The second integral represents the work done by the linear and nonlinear viscous damping forces, localized at the absorber position x_c through the Dirac delta function $\delta(x - x_c)$.

It should be noted that the term $\dot{w} + w' v_{ab} - \dot{z}$ in Eq. 7 arises from the *relative velocity* between the moving cable and the vertically suspended mass. Specifically, $\dot{w} = \frac{\partial w}{\partial t}$ is the local transverse velocity of the cable at x_c, while $w' v_{ab}$ results from applying the chain rule to the material derivative of w:

$$\frac{dw}{dt} = \frac{\partial w}{\partial t} + \frac{\partial w}{\partial x} \frac{dx_c}{dt},$$

with $\frac{dx_c}{dt} = v_{ab}$ being the horizontal speed of the absorber while the term $\dot{z}$ represents the vertical velocity of the vertically suspended mass. Together, these terms capture the relative motion across the damper, which governs energy dissipation through the viscous damper. The linear (c_l) and nonlinear (c_{nl}) damping coefficients appear in the integrand to model this dissipation consistently within Hamilton's principle. In Eq. (7), the fluctuating lift force across the conductor, f_w, is related to fluctuating lift coefficient, C_L, by the expression [38]

$$f_w = \frac{\rho_f V_f^2 D C_L}{2}\,, \tag{8}$$

where ρ_f is the fluid density, V_f is the surrounding fluid velocity, and D is a characteristic dimension such as the conductor diameter. Using the relationship between the drag force f_d and drag coefficient C_d,

$$f_d = \frac{1}{2} \rho_f V_f^2 D C_d,$$

Eq. (8) can be written as

$$f_w = \frac{f_d}{C_d} C_L\,. \tag{9}$$

Furthermore, C_L follows the equation [38]

$$C_L\left(x, t\right) = q\left(x, t\right) - \frac{2\alpha}{\omega_{sh}} \dot{w} \tag{10}$$

where q is the wake variable, α is stall-related parameter, ω_{sh} is the vortex-shedding frequency. The second component in Eq. (10), referred to as the stall term, enables the system's self-limiting behavior by producing a negative slope in the lift coefficient during large-amplitude oscillations. As described

in [38], the wake variable, $q(x,t)$, follows the nonlinear van der Pol equation.

$$\ddot{q} - \omega_{sh}\mu\left(C_{L0}^2 - 4q^2\right)\dot{q} + \omega_{sh}^2 q = \omega_{sh}\gamma\dot{w} \tag{11}$$

where μ is the damping factor, γ is the coupling term, and C_{L0} is the lift coefficient for a stationary cylinder. It should be noted that the specific values of these parameters are determined by the dynamic interaction between the conductor and the surrounding wind and can be extracted via experimental measurements.

To provide an intuitive view of the aerodynamic excitation mechanism, a schematic representation of the wake oscillator coupled to the powerline is shown in Fig. 3. As wind flows past the powerline, alternating vortex shedding induces the wake variable $q(x,t)$, modeled using a nonlinear van-der Pol oscillator that captures the self-excited and self-limiting nature of vortex-induced vibrations. The wake variable governs the fluctuating lift coefficient and the resulting distributed aerodynamic force $f_w(x,t)$ acting on the cable, while the cable's transverse velocity $w(x,t)$ simultaneously feeds back into the wake dynamics through the velocity-coupling term in Eq. (11). Additionally, the structural displacement $w(x,t)$ is further coupled to the moving absorber through the nonlinear stiffness and damping elements, enabling energy transfer from the cable to the absorber and its subsequent dissipation. This combined fluid–structure–absorber interaction ensures both the aerodynamic energy input and the nonlinear absorber-induced dissipation mechanisms.

Next, using the energy expressions and work done obtained earlier, and employing the generalized Hamilton's principle which states

$$\delta \int_{t_1}^{t_2} (\pi - T - W)dt = 0 \tag{12}$$

for each generalized coordinate $\{w, z\}$ along with the wake oscillator equation (van der Pol) from Eq. (11), the resulting equations of motion governing the beam, the moving absorber, and the fluid forces are expressed as follows:

$$EIw'''' + \rho A\ddot{w} - Pw'' = f_w - (f_c + f_{ab})\ g\ (x,t) \tag{13a}$$
$$m_c\ddot{z} - f_{ab} = 0 \tag{13b}$$
$$\ddot{q} - \omega_s\mu\left(C_{L0}^2 - 4q^2\right)\dot{q} + \omega_s^2 q = \omega_s\gamma\dot{w} \tag{13c}$$

Because the vertically suspended mass is small compared to the main system mass, and the absorber's velocity remains low, the influence of Coriolis acceleration can be disregarded. Consequently, the expressions for concentrated forces from the span-mounted mass f_c and the absorber f_{ab} along with the transverse fluid force f_w read:

$$f_c(x,t) = m_c\ \ddot{w} \tag{14a}$$
$$f_{ab}(x,t) = k\,(w-z) + k_{nl}(w-z)^3 + c\,(\dot{w}-\dot{z}) + c_{nl}(\dot{w}-\dot{z})^3 \tag{14b}$$
$$f_w(x,t) = \frac{f_0}{C_d}\left(q - \frac{2\alpha}{\omega_{sh}}\dot{w}\right) \tag{14c}$$

Furthermore, the motion of the absorber along the cable is described by four distinct location profiles, collectively represented by the function $g(x,t)$ in Eq. (13). Each profile corresponds to a specific configuration that determines whether the absorber remains fixed or moves along the span. These profiles are defined using Dirac delta and Heaviside step functions to specify the absorber's position at any given time. For clarity, the complete piecewise definition of $g(x,t)$ is provided in Eq. (15), with the four configurations listed below.

$$g(x,t) = \begin{cases} g_1(x), & \text{fixed absorber,} \\ g_2(x,t), & \text{one-way moving absorber,} \\ g_3(x,t), & \text{two-way moving absorber,} \\ g_4(x,t), & \text{double two-way moving absorbers.} \end{cases} \tag{15}$$

The four configurations are detailed below. Note that, to provide a systematic framework for isolating the effect of the absorber's nonlinearity without introducing additional variables, these configurations follow the benchmark setups adopted in prior studies [11, 14] on *linear* moving absorbers.

- **Fixed absorber** (g_1): $\delta(x-0.02l)$ This profile represents a stationary absorber located at 2% of the conductor's length, functioning as a traditional damper
- **One-Way Moving Absorber** (g_2):

$$g_2 = \begin{cases} \delta(x - v_{ab}t)\,\Theta\left(\frac{0.1l}{v_{ab}} - t\right), & 0 < t \le \frac{0.1l}{v_{ab}} \\ \delta(x - 0.1l), & t > \frac{0.1l}{v_{ab}} \end{cases}$$

This profile models an absorber that moves from left to right with a constant velocity v_{ab}, covering 10% of the conductor's length. The motion is active during $0 < t \le \frac{0.1l}{v_{ab}}$, governed by the Heaviside step function $\Theta\left(\frac{0.1l}{v_{ab}} - t\right)$. After this time, the absorber stops and behaves as a fixed absorber at 10% of the conductor's length.

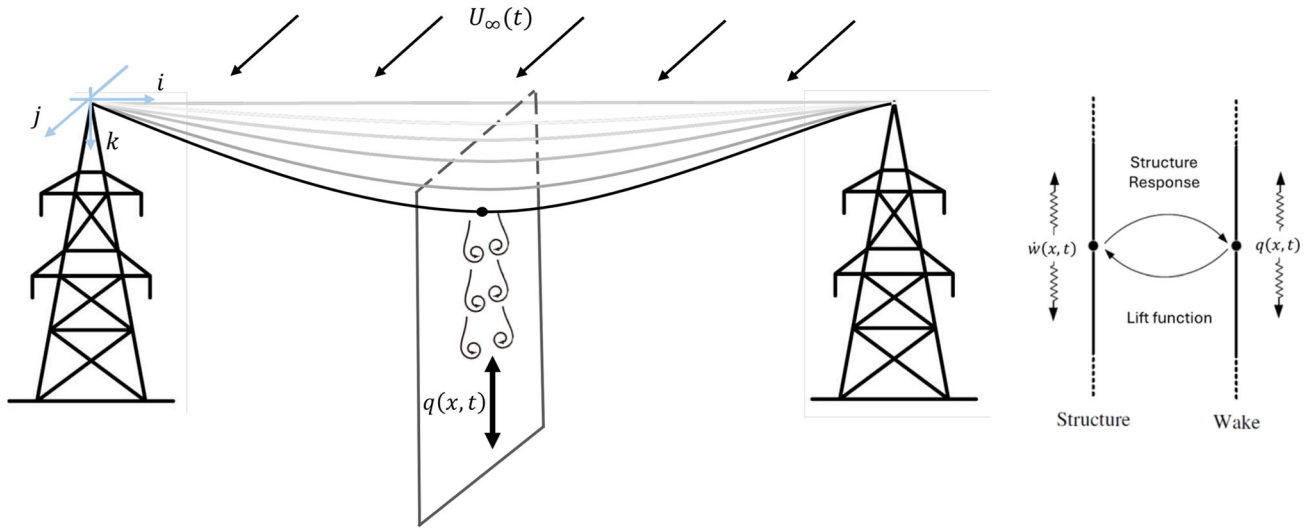

Fig. 3 Schematic representation of the bidirectional coupling between the cable motion $w(x,t)$ and the distributed wake variable $q(x,t)$ governed by the nonlinear Van der Pol oscillator

- **Two-Way Moving Absorber** (g_3):

$$= \begin{cases} \delta\left(x - v_{ab}t\right)\Theta\left(\dfrac{0.1l}{v_{ab}} - t\right) \\ +\delta\left(x - 0.1l - [0.1l - v_{ab}t]\right)\Theta\left(t - \dfrac{0.1l}{v_{ab}}\right) \\ \Theta\left(\dfrac{0.2l}{v_{ab}} - t\right) \quad 0 < t \le \frac{0.2l}{v_{ab}} \\ \delta(x) \quad t > \frac{0.2l}{v_{ab}} \end{cases}$$

This profile describes an absorber that first moves from left to right, covering 10% of the cable's length. This motion is captured by $\delta(x - v_{ab}t)\,\Theta\left(\dfrac{0.1l}{v_{ab}} - t\right)$ during $0 < t \le \dfrac{0.1l}{v_{ab}}$. After $t = \dfrac{0.1l}{v_{ab}}$, the first term becomes zero, and the second term activates, modeling the reverse motion from right to left during $\frac{0.1l}{v_{ab}} \le t < \dfrac{0.2l}{v_{ab}}$. For $t \ge \dfrac{0.2l}{v_{ab}}$, the absorber behaves as a fixed absorber at $x = 0$.

- **Double Two-Way Moving Absorbers** (g_4):

$$= \begin{cases} g_3 + \delta\left(x - [0.9l - v_{ab}t]\right)\Theta\left(\dfrac{0.1l}{v_{ab}} - t\right) \\ +\delta\left(x - l - [0.1l - v_{ab}t]\right)\Theta\left(\dfrac{0.1l}{v_{ab}} - t\right) \\ \Theta\left(\dfrac{0.2l}{v_{ab}} - t\right) \quad 0 < t \le \dfrac{0.2l}{v_{ab}} \\ \delta(x) + \delta(x - 0.9l) \quad t > \dfrac{0.2l}{v_{ab}} \end{cases}$$

This profile captures the motion of two absorbers at opposite ends of the conductor. The first absorber follows the dynamics of g_3, moving back and forth at the left end of the cable. The second absorber, located at 90% of the conductor's length, moves in a similar two-way fashion, covering 10% of the cable length from the right side. For $t \ge \dfrac{0.2l}{v_{ab}}$, both absorbers behave as fixed absorbers at their respective endpoints.

With the location profiles of the absorber established, we now define the boundary and initial conditions for the system. In this analysis, the cable is modeled with conventional boundary conditions for a simply supported configuration. The initial conditions correspond to a stationary cable, implying that:

$$\text{BCs}: \quad w(0,t) = 0,\ w(0,t) = 0,\ w''(0,t) = 0,\ w''(L,t) = 0; \tag{16a}$$

$$\text{ICs}: \quad w(x,0) = 0,\ \dot{w}(x,0) = 0,\ z(0) = 0,\ \dot{z} = 0 \tag{16b}$$

A nonzero initial condition for the wake variable q corresponds to initiating wake dynamics, which generate a wake force that induces the response of the coupled structure, leading to a realistic initiation of oscillations. Accordingly, the following initial conditions are defined for the wake oscillator:

$$q(0) \neq 0, \quad \dot{q}(0) = 0 \tag{17}$$

Different methodologies can be employed to solve the dynamical system described by Eqs. (13), (14), (16) and (17).

One widely used approach is the Galerkin projection method, which transforms the continuous PDE model into a discrete set of ordinary differential equations (ODEs). This method requires a set of basis functions which satisfy the essential boundary condition of the system. Accordingly, the solutions for $w(x,t)$ and $q(x,t)$ can be approximated as:

$$w(x,t) = \sum_{j=1}^{\infty} \phi_{wj}(x) \cdot a_j(t)$$
$$\text{and} \quad q(x,t) = \sum_{j=1}^{\infty} \phi_{qj}(x) \cdot \tilde{q}_j(t) \tag{18}$$

where $\phi_{wj}(x)$ and $\phi_{qj}(x)$ are the spatial basis functions for w and q, respectively, and $a_j(t)$ and $\tilde{q}_j(t)$ are the corresponding temporal coordinates. In the current analysis, $w(x,t)$ and $q(x,t)$ demonstrate identical mode shapes [7], implying that

$$\phi_{wj}(x) = \phi_{qj}(x) = \phi_j(x).$$

For a simply supported cable under pretension, the mode shapes $\phi_j(x)$ are given by [39]:

$$\phi_j(x) = \sqrt{\frac{2}{\rho A l}} \sin\left[\left(\sqrt{\frac{-P}{2EI} + \sqrt{\frac{P^2}{4(EI)^2} + \frac{\rho A \omega_j^2}{EI}}}\right) x\right] \tag{19}$$

where ω_j represents the natural frequencies of the bare beam and is given by

$$\omega_j = \left(\frac{\pi}{l}\right)^2 \sqrt{\frac{EI}{\rho A}\left(j^4 + \frac{j^2 Pl^2}{\pi^2 EI}\right)} \tag{20}$$

Upon substituting the assumed solution into the governing equation of motion (13), we obtain

$$\begin{aligned} EI \sum_{j=1}^{\infty} \phi_j'''' a_j - P \sum_{j=1}^{\infty} \phi_j'' a_j + \rho A \sum_{j=1}^{\infty} \phi_j \ddot{a}_j \\ = \frac{f_0}{C_d}\left(\sum_{j=1}^{\infty} \phi_j \tilde{q}_j - \frac{2\alpha}{\omega_{sh}} \sum_{j=1}^{\infty} \phi_j \dot{a}_j\right) \\ - \left[m_c \left(\sum_{j=1}^{\infty} \phi_j \ddot{a}_j\right) + k\left(\sum_{j=1}^{\infty} \{\phi_j a_j\} - z\right) \right. \\ + k_{nl}\left(\sum_{j=1}^{\infty} \{\phi_j a_j\} - z\right)\left(\sum_{m=1}^{\infty} \{\phi_m a_m\} - z\right) \\ \left.\left(\sum_{n=1}^{\infty} \{\phi_n a_n\} - z\right) + c\left(\sum_{k=1}^{\infty} \{\phi_j \dot{a}_j\} - \dot{z}\right)\right. \\ \left. + c_{nl}\left(\sum_{j=1}^{\infty} \{\phi_j \dot{a}_j\} - \dot{z}\right)\left(\sum_{m=1}^{\infty} \{\phi_m \dot{a}_m\} - \dot{z}\right)\right. \\ \left.\left(\sum_{n=1}^{\infty} \{\phi_n \dot{a}_n\} - \dot{z}\right)\right] G(x,t) \end{aligned} \tag{21}$$

while the equation of motion of the absorber becomes

$$\begin{aligned} m_{ab}\ddot{z} - k\left(\sum_{j=1}^{\infty} \{\phi_j a_j\} - z\right)_{x=x_c} \\ - k_{nl}\left[\left(\sum_{j=1}^{\infty} \{\phi_j a_j\} - z\right)\left(\sum_{m=1}^{\infty} \{\phi_m a_m\} - z\right)\right. \\ \left.\left(\sum_{n=1}^{\infty} \{\phi_n a_n\} - z\right)\right]_{x=x_c} - c\left(\sum_{k=1}^{\infty} \{\phi_j \dot{a}_j\} - \dot{z}\right)_{x=x_c} \\ - c_{nl}\left[\left(\sum_{j=1}^{\infty} \{\phi_j \dot{a}_j\} - \dot{z}\right)\right. \\ \left.\left(\sum_{m=1}^{\infty} \{\phi_m \dot{a}_m\} - \dot{z}\right)\left(\sum_{n=1}^{\infty} \{\phi_n \dot{a}_n\} - \dot{z}\right)\right]_{x=x_c} = 0 \end{aligned} \tag{22}$$

and the van der Pol oscillator equation is given by:

$$\begin{aligned} \sum_{j=1}^{\infty} \phi_j \ddot{\tilde{q}}_j - \omega_{sh}\mu\left(C_{L0}^2 - 4\sum_{j=1}^{\infty} \phi_j \tilde{q}_j \sum_{m=1}^{\infty} \phi_m \tilde{q}_m\right) \\ \sum_{n=1}^{\infty} \phi_n \dot{\tilde{q}}_n + \omega_j^2 \sum_{j=1}^{\infty} \phi_j \tilde{q}_j \\ = \omega_{sh}\gamma \sum_{j=1}^{\infty} \phi_j \dot{a}_j \end{aligned} \tag{23}$$

Since the assumed forms of the solutions are not exact solutions to the system, Eqs. (21), (22) and (23) are not satisfied identically, resulting in residual errors. To minimize these residuals, we apply the standard Galerkin projection method and use the following identities:

$$\begin{aligned} \int_0^l \phi_k \left[\frac{d^2}{dx^2}\left(EI\frac{d^2\phi_j(x)}{dx^2}\right) - \frac{d}{dx}\left(P\frac{d\phi_j(x)}{dx}\right)\right] dx \\ = \omega_j^2 \delta_{jk} \\ = \begin{cases} \omega_j^2 & j = k \\ 0 & j \neq k \end{cases} \end{aligned} \tag{24a}$$

$$\int_0^l \rho A \phi_k(x)\phi_j(x)\,dx = \delta_{jk} = \begin{cases} 1 & j = k \\ 0 & j \neq k \end{cases} \tag{24b}$$

$$\int_0^l \phi_k^2(x)\phi_j^2(x)\,dx \tag{24c}$$

$$= \begin{cases} \frac{\hat{f}^4}{\theta_j}\left[\frac{3}{8}\left(l\theta_j - \frac{1}{2}\sin\left(l\theta_j\right)\right) - \frac{1}{4}\sin^3\left(l\theta_j\right)\cos\left(l\theta_j\right)\right] & j = k \\ \hat{f}^4\left[\frac{l}{4}\cos\left(2l\theta_j\right) + \frac{l}{2}\sin^2\left(l\theta_j\right) - \frac{1}{8\theta_j}\sin^2\left(l\theta_j\right)\sin\left(4l\theta_j\right)\right. & \\ \left. -\frac{3}{32\theta_j}\sin\left(2l\theta_j\right) - \frac{1}{96\theta_j}\sin\left(6l\theta_j\right)\right] & j \neq k \end{cases} \tag{24d}$$

where

$$\hat{f} = \sqrt{\frac{2}{ml}} \quad \text{and} \quad \theta_j = \sqrt{\frac{-P}{2EI} + \sqrt{\frac{P^2}{4(EI)^2} + \frac{\rho A \omega_j^2}{EI}}} \tag{25}$$

to get

$$\begin{aligned} &\ddot{a}_k + 2\zeta\omega_k\dot{a}_k + \omega_k^2 a_k + \left[m_c\left(\sum_{j=1}^{\infty}\phi_j\ddot{a}_j\right)\right. \\ &+ k\left(\sum_{j=1}^{\infty}\{\phi_j a_j\} - z\right) \\ &+ c\left(\sum_{j=1}^{\infty}\{\phi_j\dot{a}_j\} - \dot{z}\right) \\ &+ k_{nl}\left(\sum_{j=1}^{\infty}\{\phi_j a_j\} - z\right)\left(\sum_{m=1}^{\infty}\{\phi_m a_m\} - z\right) \\ &\left(\sum_{n=1}^{\infty}\{\phi_n a_n\} - z\right) + c_{nl}\left(\sum_{j=1}^{\infty}\{\phi_j\dot{a}_j\} - \dot{z}\right) \\ &\left.\left(\sum_{m=1}^{\infty}\{\phi_m\dot{a}_m\} - \dot{z}\right)\left(\sum_{n=1}^{\infty}\{\phi_n\dot{a}_n\} - \dot{z}\right)\right]_{x=x_c} \end{aligned} \tag{26a}$$

$$\tilde{g}_k(t) = \frac{f_0}{C_d\rho A}\left(\tilde{q}_k - \frac{2\alpha}{\omega_{sh}}\dot{a}_k\right)$$

$$\begin{aligned} &m_{ab}\ddot{z} - \left[k\left(\sum_{j=1}^{\infty}\{\phi_j a_j\} - z\right) + k_{nl}\left(\sum_{j=1}^{\infty}\{\phi_j a_j\} - z\right)\right. \\ &\left(\sum_{m=1}^{\infty}\{\phi_m a_m\} - z\right)\left(\sum_{n=1}^{\infty}\{\phi_n a_n\} - z\right) \\ &+ c\left(\sum_{j=1}^{\infty}\{\phi_j\dot{a}_j\} - \dot{z}\right) + c_{nl}\left(\sum_{j=1}^{\infty}\{\phi_j\dot{a}_j\} - \dot{z}\right) \\ &\left.\left(\sum_{m=1}^{\infty}\{\phi_m\dot{a}_m\} - \dot{z}\right)\left(\sum_{n=1}^{\infty}\{\phi_n\dot{a}_n\} - \dot{z}\right)\right]_{x=x_c} \\ &= 0 \end{aligned} \tag{26b}$$

$$\begin{aligned} &\ddot{\tilde{q}}_k - \omega_{sh}\mu C_{L0}^2\dot{\tilde{q}}_k + 4\rho A\omega_k\mu \\ &\left(\sum_{j=1}^{\infty}\dot{\tilde{q}}_k\cdot\tilde{q}_j^2\int_0^l\phi_k^2\cdot\phi_j^2\,dx + 2\sum_{\substack{j=1\\ j\neq k}}^{\infty}\tilde{q}_k\tilde{q}_j\dot{\tilde{q}}_j\int_0^l\phi_k^2\cdot\phi_j^2\,dx\right) \\ &+ \omega_{sh}^2\tilde{q}_k = \omega_{sh}\gamma\dot{a}_k \end{aligned} \tag{26c}$$

for $k = 1..N$. In the above equation ζ represents the damping coefficient for the cable. Moreover, in Eq. (26) $\tilde{g}_k(t)$ is defined as

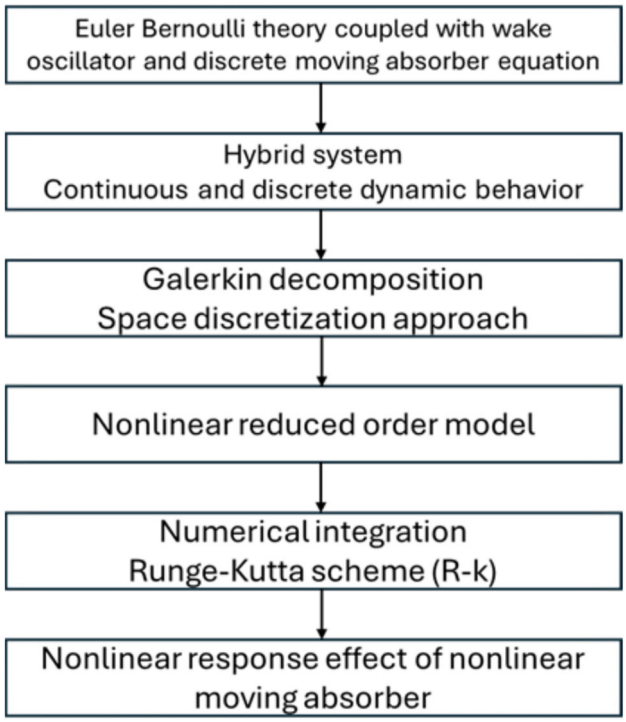

Fig. 4 Modeling approach and analysis of a powerline equipped with a nonlinear moving absorber under wind forces

$$\tilde{g}_k(t) = \int_0^l \phi_k(x)\, g(x,t)\, dx \tag{27}$$

A flowchart outlining the main steps of the model development is provided in Fig. 4. The formulation begins with the governing equations of an Euler–Bernoulli cable coupled to a nonlinear wake oscillator and a nonlinear moving absorber. These equations are reduced via a Galerkin projection to obtain a finite set of coupled nonlinear ordinary differential equations. Numerical integration of this reduced-order model is then used to examine the nonlinear dynamics of the cable–wake–absorber system for different absorber configurations, speeds, and parameter sets.

To evaluate the efficacy of the proposed nonlinear vibration absorber, we define the energy dissipation index η as the ratio of dissipated energy E_d to input energy E_{in}

$$\eta = \frac{E_d}{E_{in}}. \tag{28}$$

Here E_{in}, represents the total input energy supplied to the beam by the force f_w, which acts at a location x_f along the length of cable. It is expressed as

$$E_{in} = \int_0^{t_0}\int_0^l \left\{ f_w(x,t)\left[\sum_{i=1}^{\infty}\Phi(x)\,\dot{a}(t)\right]_{x=x_f}\right\} dx\, dt\,. \tag{29}$$

Table 1 Structural properties of cable, absorber, and van-der Pol oscillator

Parameter	Unit	Value	Parameter	Unit	Value
l	m	27.25	F_0	N/m	0.4320
EI	N-m^2	1602	ω_1	rad	15.0734
ρA	kg/m	1.6286	m_a	kg	4.8
P	N/m	27840	v_{ab}	m/s	0.1
m_c	kg	0.2	α	–	0
k	N/m	1356.96	C_{L0}	–	0.28
c	N-s/m	177.0	c_d	–	1

Similarly E_d, the energy dissipated by the linear an nonlinear damping elements of the moving absorber and is given by

$$E_d = \int_0^{t_1} \left\{ c \left[\dot{z}(t) - \sum_{j=1}^{\infty} \left\{ \phi_j(x)\, \dot{a}_j(t) \right\} \right]^2 + c_{nl} \left[\dot{z}(t) - \sum_{j=1}^{\infty} \left\{ \phi_j(x)\, \dot{a}_j(t) \right\} \right]^4 \right\}_{x=x_c} dt \tag{30}$$

In the above expressions, t_0 is the duration for which f_w is applied and the t_1 is the large enough time to ensure that transient dynamics are nearly damped.

2.1 Convergence of the Galerkin approximation

Before proceeding with the numerical simulation of the system, it is necessary to select an appropriate truncation level for the Galerkin approximation of $w(x,t)$ and $q(x,t)$. To achieve this, we analyze the Bode plot of the bare beam, using the structural properties listed in Table 1 [2, 14]. The Bode plot for different numbers of terms in the expansion is presented in Fig. 5.

From Fig. 5, it is evident that the Bode plots for $N = 5$ and $N = 10$ terms in the expansion closely match for lower modes, further implying that $N = 5$ is sufficient to capture the system's primary dynamics in these modes. However, for higher modes, a larger number of terms is required to accurately capture the peaks and the associated dynamic response. Since the current analysis focuses on the system's response dominated by the first few modes, selecting $N = 5$ for the approximation provides sufficient accuracy while maintaining computational efficiency.

In the next section, we present results on the dynamic behavior of the system and the corresponding frequency response curve.

3 Numerical results and analysis

This section analyzes the dynamic characteristics of the conductor integrated with a nonlinear vibration absorber, with the aerodynamic forces represented through a wake oscillator model. Before analyzing the system's response for various system parameter combinations, it is necessary to identify the parameters of the semi-empirical wake oscillator model. Specifically, the key parameters μ and γ are determined by comparing the response of the current model with experimental results reported in earlier studies. Bukhari et al. [14] analyzed the dynamics of the conductor with a moving absorber using a sinusoidal model for the lift force based on experimental data [31, 40]. In the current analysis, these parameters are identified by comparing the response of the coupled beam–oscillator model against that of the sinusoidal model at a given frequency.

To achieve this, we first set the stall term (α) to zero to ensure that damping in the system arises solely from the structural damping of the conductor and the moving vibration absorber. Additionally, the excitation amplitude of the harmonic forcing is scaled using the steady-state behaviour of the wake variable q over a given frequency range. Next, the numerical values of μ and γ are determined by matching the midpoint motion of the conductor between the wake oscillator model and the harmonic model.For this analysis, a one-way moving absorber is considered, with a constant velocity $v_{ab} = 0.1m/s$, while the conductor is excited at a frequency $f = 20$ Hz. The time-domain response of both models shows good agreement for parameter values of $\gamma = 1.2534 \times 10^{-2}$ and $\mu = 0.3763$, as depicted in Fig. 6. Therefore, the identified parameter values are used in the subsequent analysis unless otherwise specified.

Next, we evaluate the system's frequency behavior under the wake oscillator model versus the sinusoidal model for the lift force. This step also serves to highlight the motivation behind the current analysis. The frequency response curve, shown in Fig. 7, reveals a significant difference between the two models at the resonance at $f_1 = 2.399Hz$. More specifically, the sinusoidal model fails to capture the effect of nonlinearity at resonance, whereas the van der Pol oscillator demonstrates hardening nonlinearity at resonance. This behavior can be attributed to the velocity-dependent damping term in the van der Pol oscillator, which is quadratic in nature. Capturing such nonlinear effects is essential for accurately representing the dynamics of the current nonlinear system, making the self-excited nonlinear oscillator a suitable choice for modeling the aerodynamic lift force.

In this section, our focus shifts towards numerical simulations, aiming to fulfill several key objectives. Firstly, we intend to compare the time responses of different location profiles, $G(x,t)$ associated with both linear and nonlinear absorbers. Secondly, our goal is to examine how different

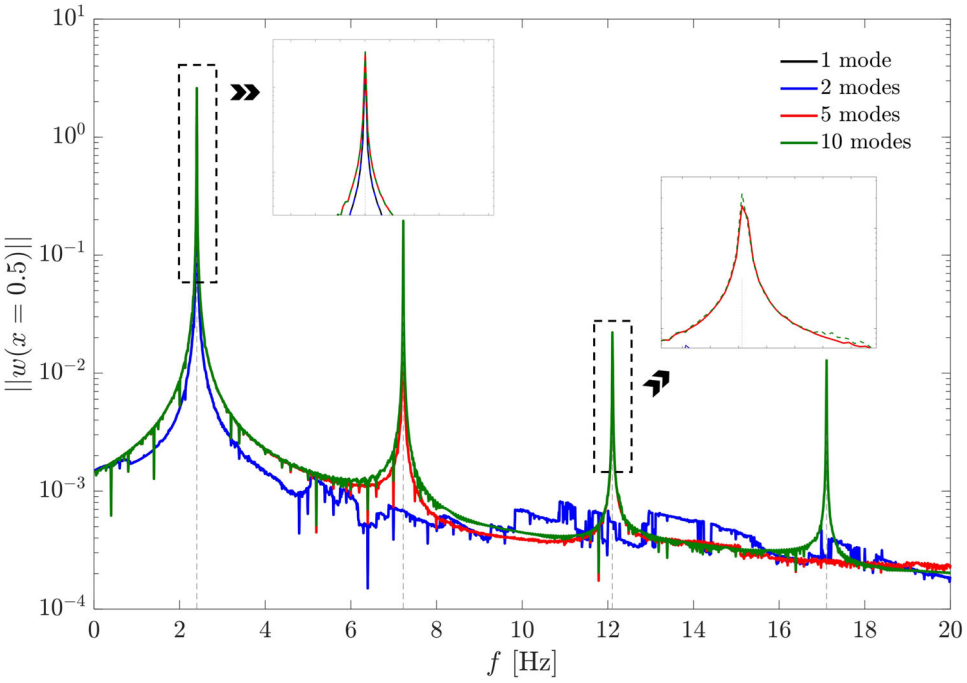

Fig. 5 Convergence analysis of the Bode plot for the bare beam using reduced models with $N = 1, 2, 5$ and 10 modes

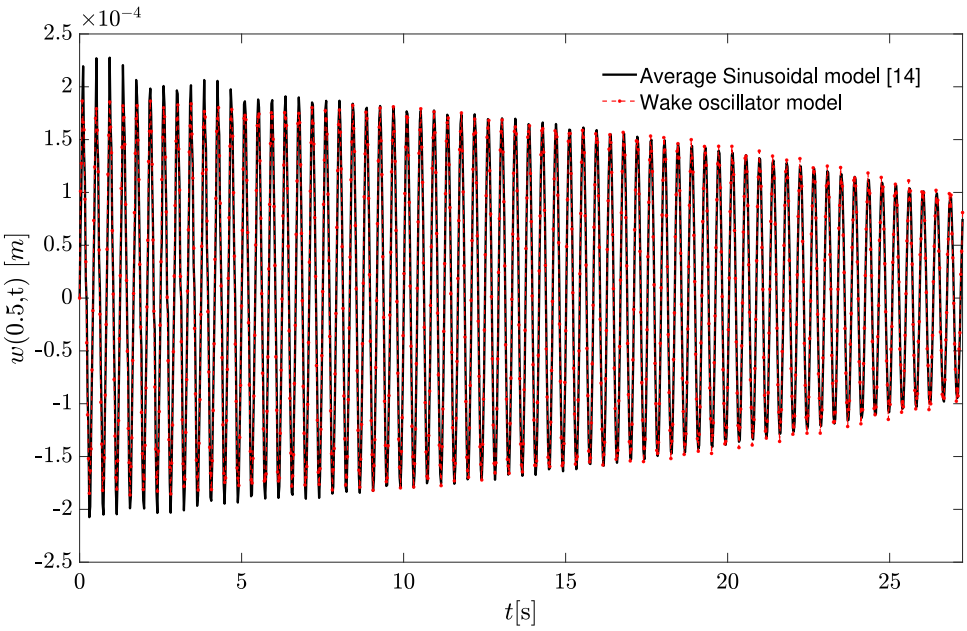

Fig. 6 Comparison of the time responses obtained using two different force models at 20 Hz

parameters influence the overall system response. Lastly, an assessment of the efficiency of the nonlinear absorber based on the portion of the wind energy dissipated, seeking to identify the optimal placement location. To maintain alignment with empirical data, we adhere to the structural and fluid properties outlined in the referenced experiments [2], with concise details provided in Table 1 as per [14].

With the values of μ and γ identified, we now present the temporal behavior of the system for the various location profiles discussed earlier, considering both linear and nonlinear moving dampers. This analysis evaluates the effectiveness of the nonlinear moving absorber in comparison to its linear counterparts.

3.1 Time response for absorber profiles

In this section, we assess the performance of the nonlinear vibration absorber compared to its linear counterpart across various location profiles, $G(x, t)$. For this purpose, we examine the time response of the conductor's midspan, $w(0.5, t)$, over the time interval required for the absorber to complete its motion. These time histories are shown in Figs. 8, 9, 10,

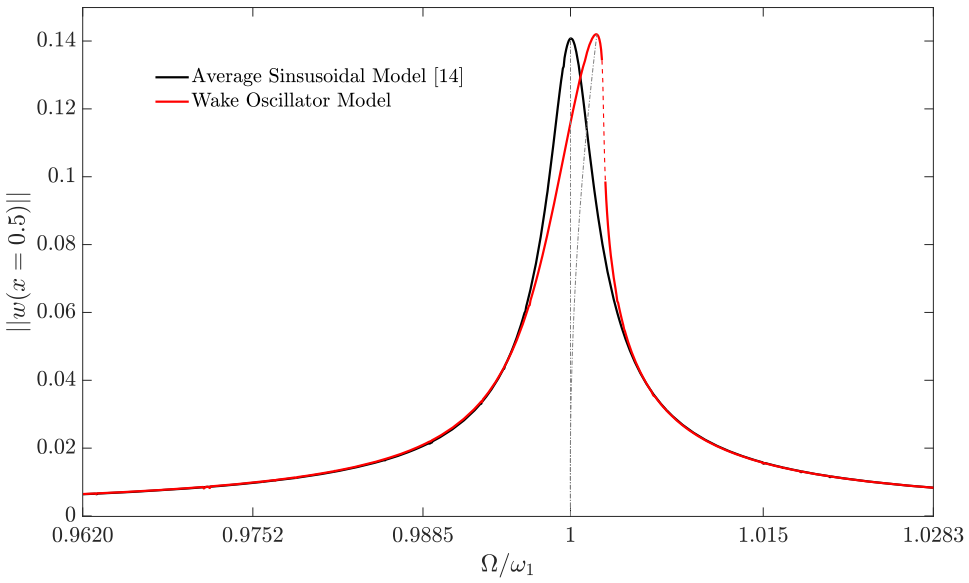

Fig. 7 Analysis of the frequency behavior of the cable near the first natural frequency using two force models

and 11, corresponding to the location profiles g_1, g_2, g_3, and g_4, respectively. For this numerical analysis, we use the parameter values for the linear vibration absorber listed in Table 1, while for the nonlinear vibration absorber, we use $k = 1356.96$, $c = 0$, $k_{nl} = 1356.96$ and $c_{nl} = 177$, unless stated otherwise. Additionally, for all location profiles, the conductor is excited near its first natural frequency $f_1 = 2.415$ Hz.

Figure 8 illustrates the midspan displacement for the fixed absorber profile g_1, comparing the performance of linear and nonlinear vibration absorbers. Based on Fig. 8, it is evident that the vibration amplitude w at midspan corresponding to the nonlinear vibration absorber remains significantly lower than that of its linear counterpart. This observation arises due to, at resonance, the system reaches its maximum amplitude, which leads to a more significant increase in the damping force provided by the nonlinear absorber.

Although the midspan vibration amplitude for the fixed absorber profile is reduced with the implementation of a nonlinear vibration absorber compared to the linear counterpart, it still remains relatively high. This observation motivates further exploration of other methodologies, including moving vibration absorbers, to achieve more effective vibration suppression.

To evaluate the performance of the moving vibration absorber, We investigate the midspan response of the conductor with a nonlinear absorber in contrast to the linear configuration, based on the location profile g_2 (one-way moving absorber). For completeness, we also include a comparison with the fixed vibration absorber, as shown in Fig. 9. As noted earlier, the vibration absorber in profile g_2 moves forward along the conductor and ceases motion after completing its course. From Fig. 9, it is observed that while the moving linear absorber reduces the vibration amplitude compared to the fixed absorber, the performance of the absorber can be improved significantly by including nonlinear elements in it. This enhanced performance of the absorber is attributed to the ability of the moving absorber to traverse to more effective locations along the conductor, which is not attainable in the fixed absorber.

Next, we assess the performance of linear and nonlinear absorbers for the third location profile g_3 (two-way moving absorber). The corresponding time histories for the midspan are compared against the fixed absorber and are presented in Fig. 10. From Fig. 10, it is evident that the moving nonlinear absorber demonstrates greater effectiveness than the moving linear and fixed absorbers. Specifically, at resonance, the maximum vibration amplitude is reduced to less than half of that observed with the fixed linear absorber, and this occurs over a time period that is half as long as that of the one-way moving absorber. We emphasize that the cable response does not diminish entirely, as the van der Pol oscillator exhibits limit cycle oscillations due to its nonlinear damping characteristics.

Finally, we compare the performance of linear and nonlinear absorbers for the fourth location profile g_4, which involves two two-way moving absorbers covering 10% of the conductor's length (27.5 m) on both sides. The correspoding time histories are presented in Fig. 11. From Fig. 11, it is evident that there is a further decrease in vibration amplitude compared to other location profiles. As with the other profiles, the nonlinear absorber is more effective than its linear counterpart for profile g_4. Additionally, the inclusion of an extra nonlinear absorber leads to pronounced nonlinearities in the system, causing some fluctuations in the response before the system settles into a limit cycle.

To this end, we emphasize that at resonance and with an appropriate choice of system parameters, including absorber

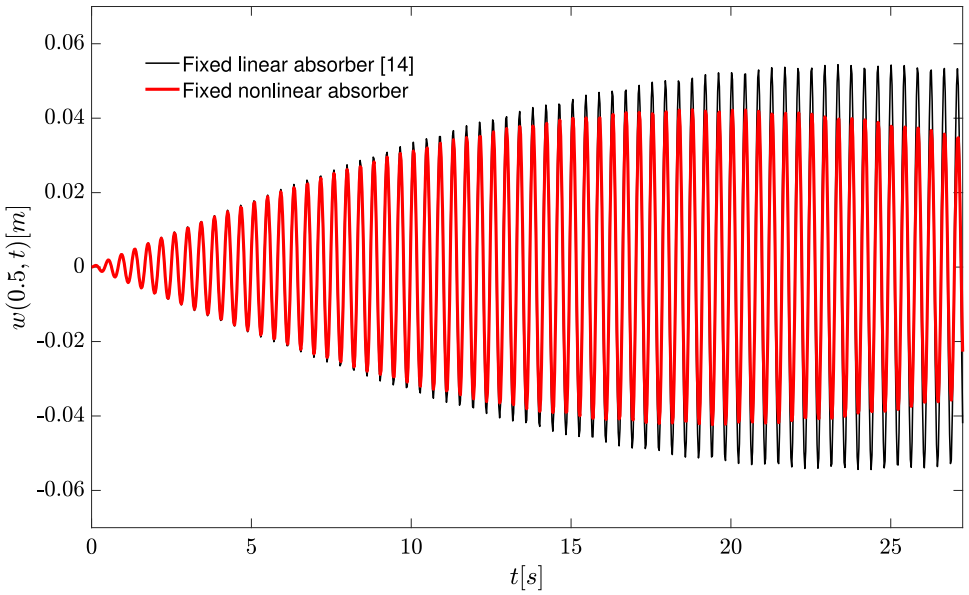

Fig. 8 Time response comparison at mid-span between a fixed linear absorber and a corresponding nonlinear configuration at $f = 2.415$ Hz

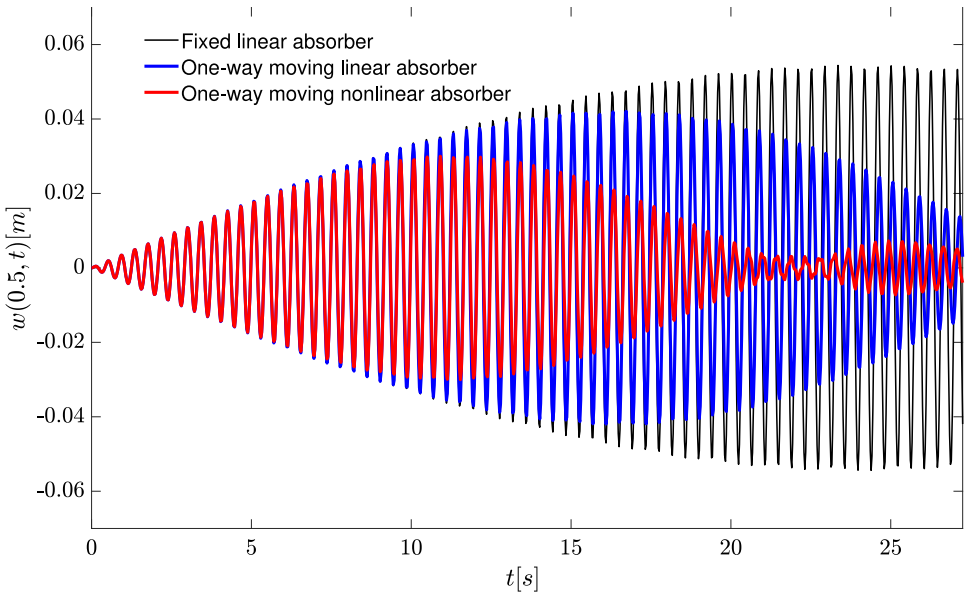

Fig. 9 Comparison of midspan time response of the conductor for fixed nonlinear, one-way linear, and one-way nonlinear vibration absorbers at $f = 2.414$ Hz

velocity, nonlinear stiffness, damping, and van der Pol parameters, the nonlinear moving absorber outperforms its linear counterpart in mitigating cable vibrations. Accordingly, a parametric analysis is conducted and presented next.

3.2 Influence of the main parameters on the system behavior

In this section, we examine the influence of various system parameters on the cable's behavior. These include absorber parameters such as nonlinear stiffness, nonlinear damping, velocity, and weight distribution, as well as van der Pol oscillator parameters, including the coupling term, damping coefficient, and stall term. This analysis aims to identify the key parameters and their optimal values for effective vibration mitigation.

We begin by examining the impact of the velocity of the nonlinear moving absorber. Increased absorber velocity can influence resonance effects, thereby affecting the rate of energy dissipation. However, excessively high velocities can also lead to material fatigue, degradation, and potential structural damage over time. Therefore, in the analysis, we restrict ourselves to moderate velocity of the absorber ranging from 0.1 m/s to 1 m/s, across excitation frequencies from 0 Hz to 20 Hz. The results, presented as a contour plot in Fig. 12aA 3D plot illustrating the variation of maximum displacement at the midspan of the cable with varying absorber velocity and frequency is shown in Fig. 12b

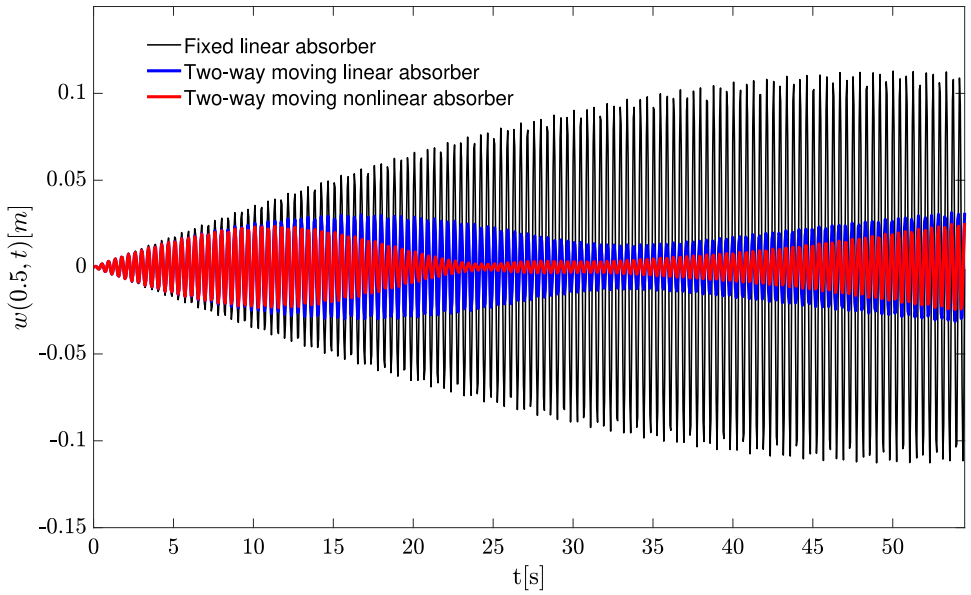

Fig. 10 Comparison of midspan time response of the conductor for fixed nonlinear, two-way linear, and two-way nonlinear vibration absorbers at $f = 2.415$ Hz

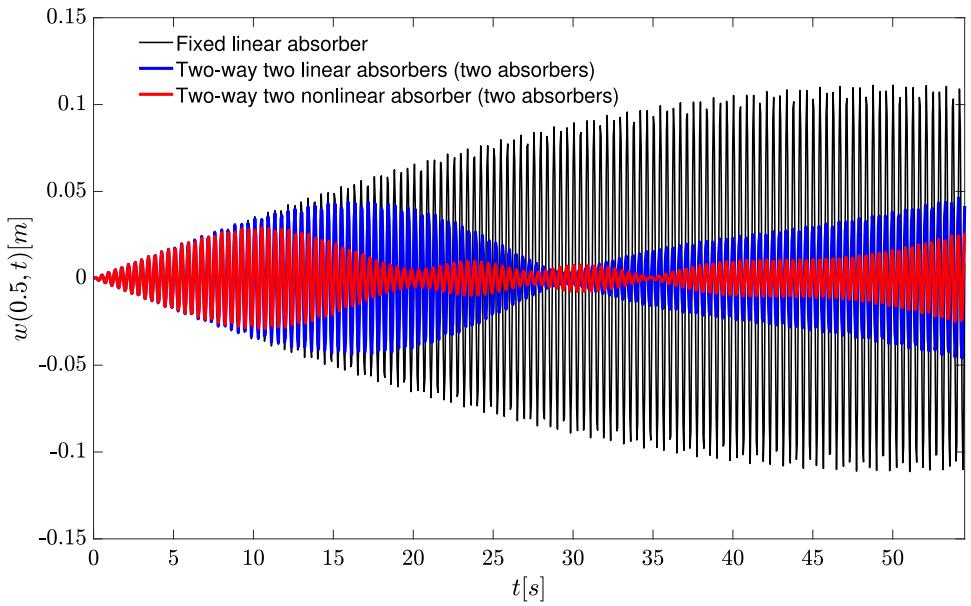

Fig. 11 Comparison of midspan time response of the conductor for fixed nonlinear, two two-way linear, and two two-way nonlinear vibration absorbers at $f = 2.415$ Hz

Next, we examine the effect of nonlinear stiffness and damping on the maximum vibration amplitude and compare it against the linear absorber. A 3D plot illustrating the normalized maximum displacement of the midspan (relative to the maximum displacement of the mid-span corresponding to the linear absorber) is shown in Fig. 13 for various nonlinear stiffness and damping coefficient values at $f = 2.399$ Hz. For this analysis, the absorber's position is fixed at 2% of the conductor's length. From Fig. 13, we observe that an increase in nonlinear damping results in a significant reduction in the maximum amplitude. In contrast, changes in nonlinear stiffness have a less pronounced effect on the maximum amplitude. Furthermore, for the given values of other system parameters, critical values of nonlinear stiffness and damping exist below which the linear absorber is more effective in reducing vibrations. This observation highlights the importance of carefully selecting nonlinear stiffness and damping values to ensure efficient vibration suppression.

Having established the effects of absorber velocity, nonlinear stiffness, and damping, we now investigate the influence of weight distribution between the span-mounted mass and the vertically suspended mass of the absorber. To quantify this effect, we introduce the mass ratio β, defined as the ratio of the span-mounted mass to the total mass of the absorber. A thorough understanding of the mass ratios' effect on the system's long-term performance and reliability is essential, as an improper selection of β can lead to system instability, excessive stress on components, and

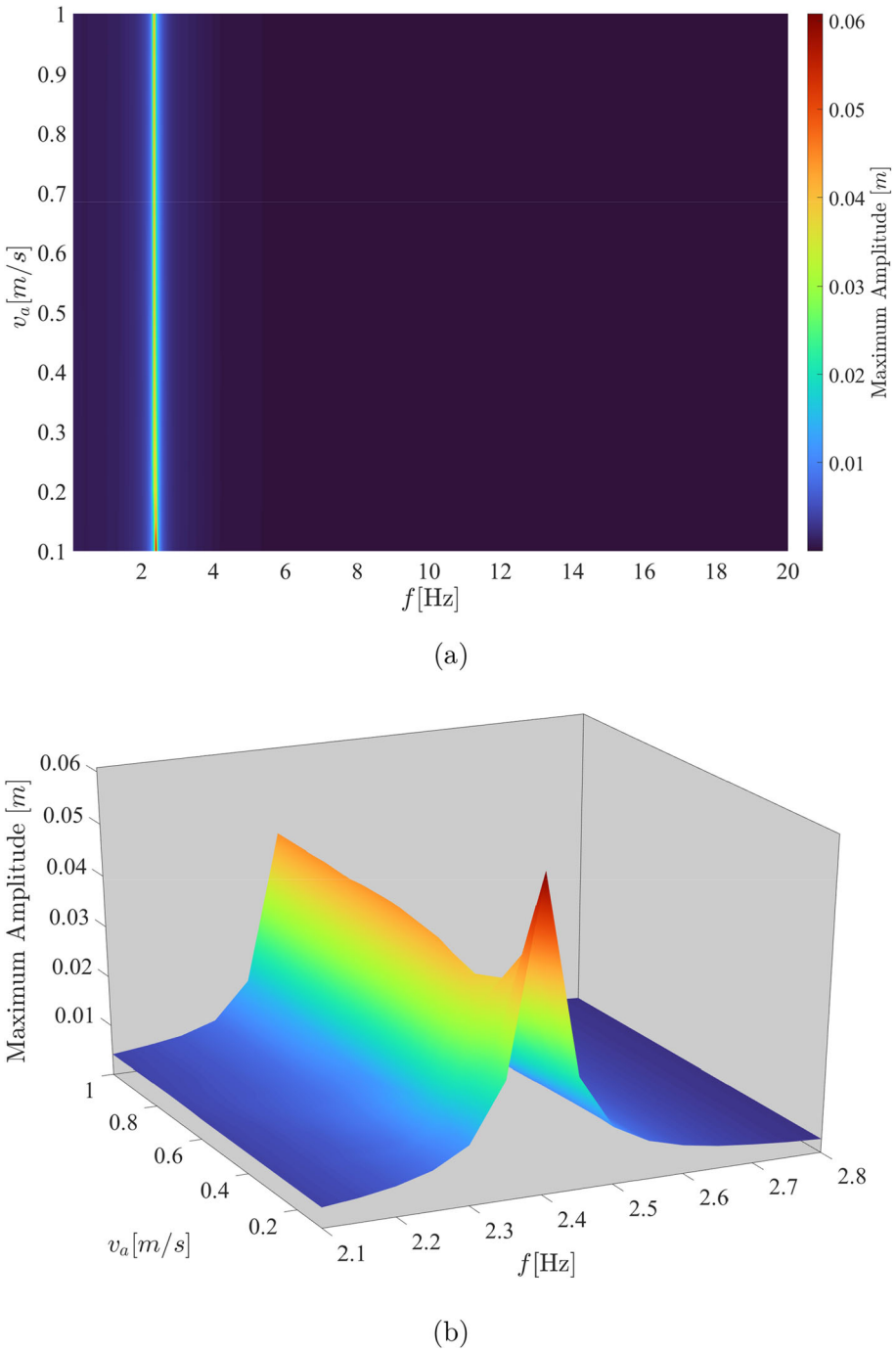

Fig. 12 (a) Maximum displacement under varying absorber velocities and excitation frequencies. (b) 3-D zoomed view of (a) in the frequency range of 2.1-to 2.8 Hz

reduced absorber effectiveness over time. For this analysis, the absorber is placed at 10% of the conductor's length, with $k_{nl} = 1000$ N/m^3 and $c_{nl} = 1000$ N-s^3/m^3. The steady-state response for different mass ratio values is presented in Fig. 14. From Fig. 14, we find that lower mass ratios correspond to reduced steady-state displacement, suggesting that a lighter span-mounted mass and heavier vertically suspended mass, for a given total absorber mass, are more effective for vibration suppression. However, increasing the vertically suspended mass could lead to system instability during operation. Additionally, a heavier vertically suspended mass is likely to require greater energy consumption to move between positions, which may impact the system's efficiency. Therefore, careful selection of the mass ratio β is crucial to achieving enhanced absorber performance while maintaining system stability and energy efficiency.

After examining the effects of absorber parameters, we now investigate the influence of the van der Pol oscillator

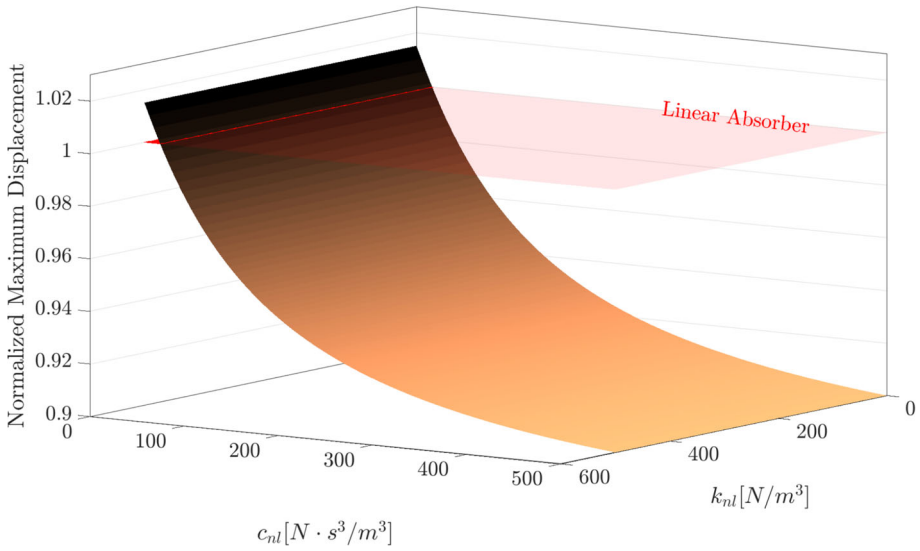

Fig. 13 Comparison of maximum beam displacement: varying Nonlinear stiffness and damping against linear absorber

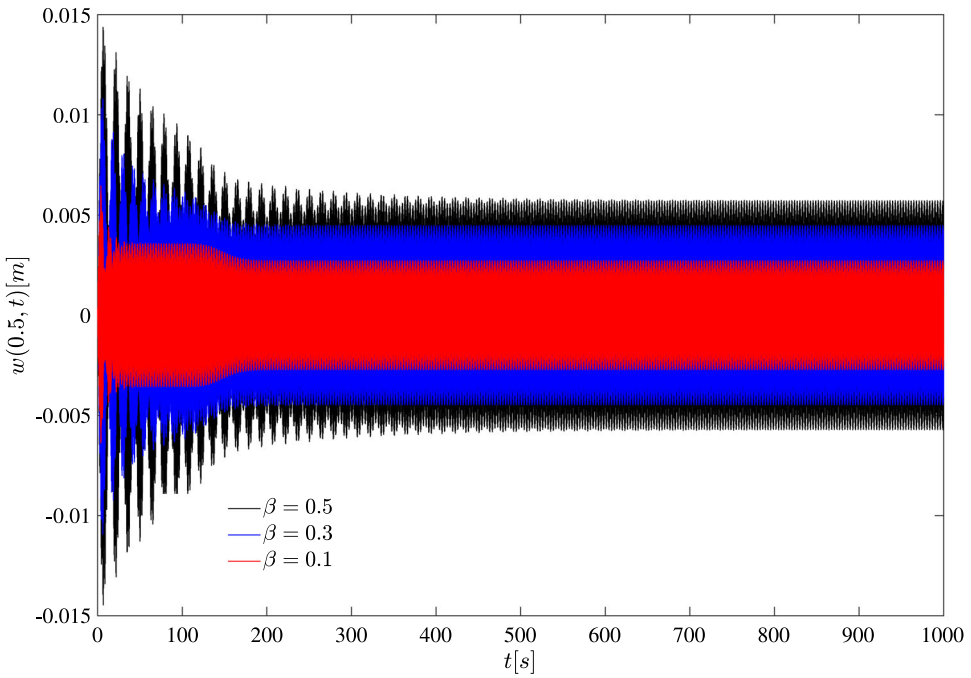

Fig. 14 Time response at the midspan of the cable for different mass ratio

parameters on the system dynamics. For this analysis, the frequency response curve at the first natural frequency of the system is utilized.

We begin by analyzing how the coupling coefficient γ, affects the response system as shown in Fig. 15. From Fig. 15, it is evident that as γ increases, both the nonlinearity and the maximum amplitude at resonance also increase. This behavior can be attributed to the fact that higher values of γ enhance energy transfer between the cable and the wake oscillator. This intensified energy exchange amplifies nonlinear effects, such as amplitude-dependent stiffness and damping, which in turn lead to complex nonlinear dynamics at resonance, including a more pronounced jump phenomenon.

Next, we examine the effect of the damping coefficient μ on the frequency response near the first natural frequency, as depicted in Fig. 16. As expected, increasing μ reduces the resonant amplitude. Interestingly, while higher damping coefficients introduce greater nonlinearity into the system, they also enhance the system's stability. This stabilization is evident from the reduced jump phenomena observed in the frequency response curves.

Finally, the effect of the stall parameter α is analyzed, as illustrated in Fig. 17. It can be observed from Fig. 17 that increasing α leads to a reduction in the maximum steady-state amplitude. This behavior can be explained using Eq. (14)c, where the stall term is coupled with the cable velocity.

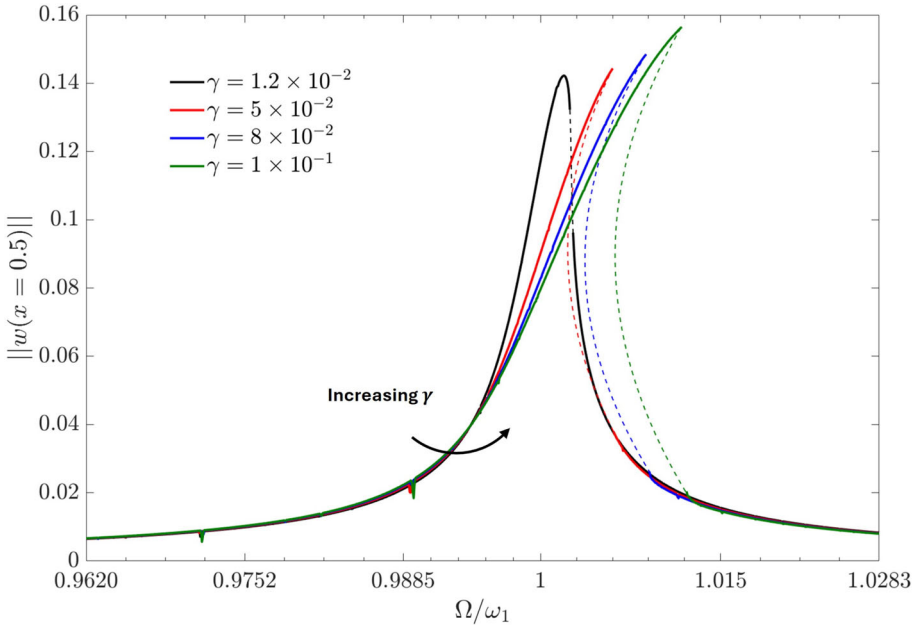

Fig. 15 Influence of different coupling coefficient γ on the frequency response curves

A higher α effectively increases the system's damping, which in turn lowers the peak steady-state amplitude and diminishes the overall nonlinearity of the system.

Having investigated the influence of various system parameters on the cable's response, the subsequent section evaluates the performance of the nonlinear moving absorber with a focus on energy efficiency.

3.3 Performance of the nonlinear absorber based on its efficiency

As previously mentioned, one way to quantify the effectiveness of the nonlinear moving vibration absorber is by evaluating its ability to dissipate input energy at resonance. The efficiency of the nonlinear moving absorber is calculated using Eqs. (28)–(29).

For this analysis, a half-sinusoidal pulse is used as the input force, consistent with prior studies [31, 41]. To validate the accuracy of the current model under half-sine pulse excitation, Fig. 18 presents a comparison between the results of the current model and those reported by Georgiades and Vakakis [41]. The comparison shows good agreement, demonstrating the reliability of the present model. With this validation, the efficiency of the nonlinear moving absorber of the current system is evaluated by considering the following impulsive excitation force

$$f(t) = \begin{cases} 0.432\sin(2\pi t/T), & 0 \le t < T/2 \\ 0, & t < 0 \text{ and } t \ge T/2 \end{cases} \quad (31)$$

where $T = f_n = 2.399$ Hz. Figure 19 illustrates the fraction of energy (η) dissipated by the linear and nonlinear absorbers for different normalized absorber positions (d/l). The linear absorber is characterized by $k = 1000$ N/m and $c = 1000$ N-s/m, while the non-linear stiffness and damping for the nonlinear absorber are $k_{nl} = 1000$ N/m^3 and $c_{nl} = 1000$ N-$(s/m)^3$. The excitation force is applied at $x_f = 30\%$ of the conductor's length. The numerical simulations depicted in Fig. 19 were performed up to t=150 s, which is sufficient for the transient dynamics to subside. Accordingly, the maximal energy dissipation ($\eta_t >> 1$) was nearly attained. From Fig. 19, it is evident that the dissipated energy is highly sensitive to the absorber's location. Higher efficiency values are observed when the absorber is positioned close to the beam's midpoint, whereas efficiency decreases markedly near the beam ends. Additionally, the nonlinear absorber consistently outperforms its linear counterpart across all locations. These results demonstrate that a properly designed and optimally located nonlinear absorber can effectively capture and dissipate a large fraction of the energy induced in the beam. Furthermore, the energy dissipation is irreversible due to the inherent nonlinearity, as reflected by the considerable energy absorbed by the nonlinear damper component of the nonlinear vibration absorber.

3.4 Practical considerations and implementation prospects

While the present study focuses on the theoretical and numerical investigation of nonlinear moving absorbers, it is important to briefly discuss their practical prospects and challenges in real transmission-line systems. Compared with traditional fixed Stockbridge dampers, a nonlinear moving absorber offers several potential advantages, including the

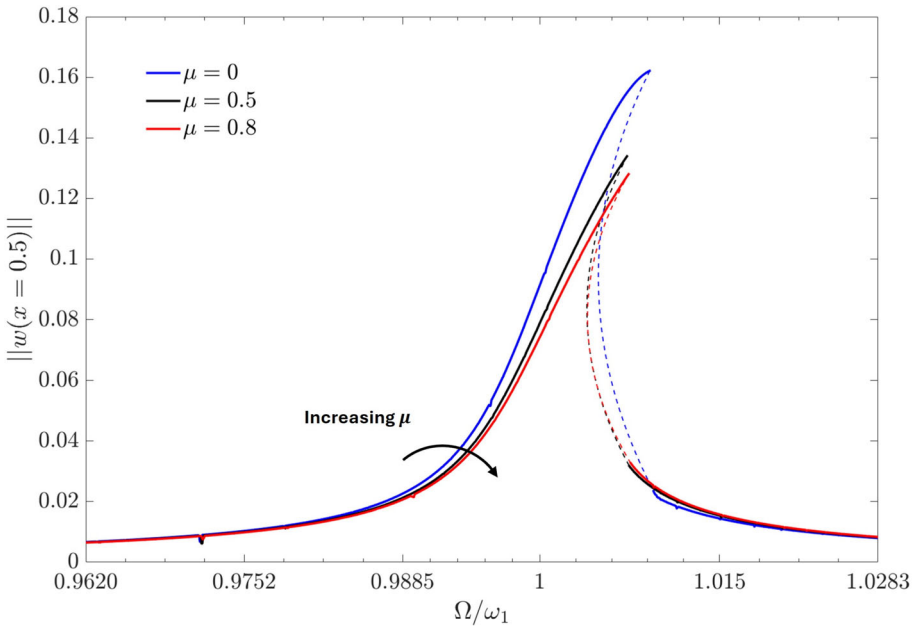

Fig. 16 Influence of different values of wake oscillator damping, μ on the frequency response curves

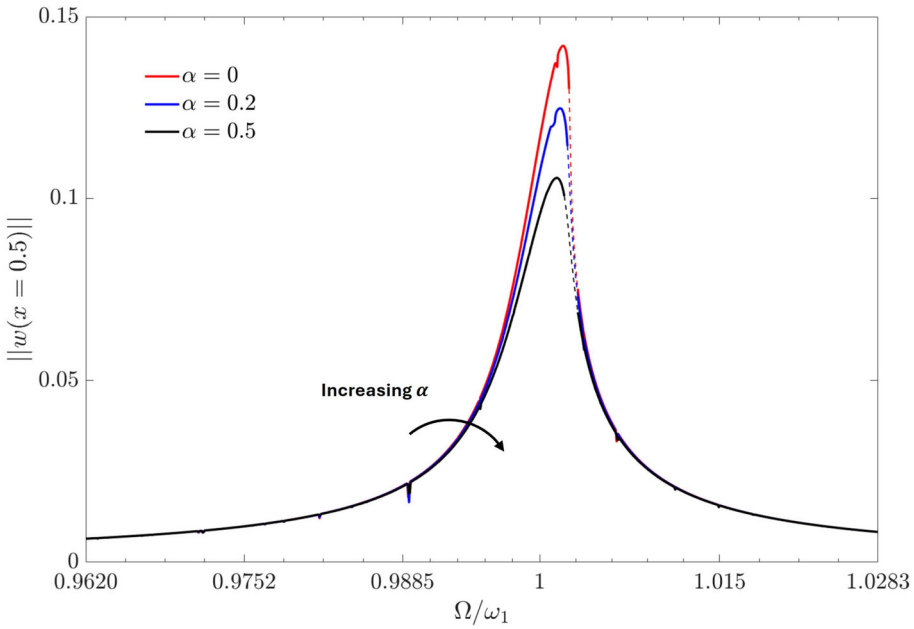

Fig. 17 Influence of different values of stall parameter, α, on the frequency response curves

ability to avoid nodal locations, adapt to spatially varying wind fields, and maintain effective energy exchange over a wider range of operating conditions due to its inherent nonlinear characteristics. These features make the concept promising for mitigating aeolian vibrations under variable or transient wind environments.

From an engineering standpoint, several implementation challenges must be addressed. A moving absorber requires a reliable mechanical guidance system capable of operating under outdoor conditions, ice loading, and long-term wear. The introduction of nonlinear stiffness and damping components increases design complexity and cost relative to conventional passive devices. Furthermore, regular inspection and maintenance procedures would need to be adapted to account for a mobile device operating along a conductor span. Integration with existing transmission-line hardware, such as spacers and suspension clamps, also requires careful consideration.

Despite these challenges, the growing interest in mobile inspection robots, autonomous monitoring devices, and adaptive damping systems suggests that moving absorbers, particularly nonlinear configurations, may become increasingly viable as supporting technologies mature. Future improvements may include lightweight composite hous-

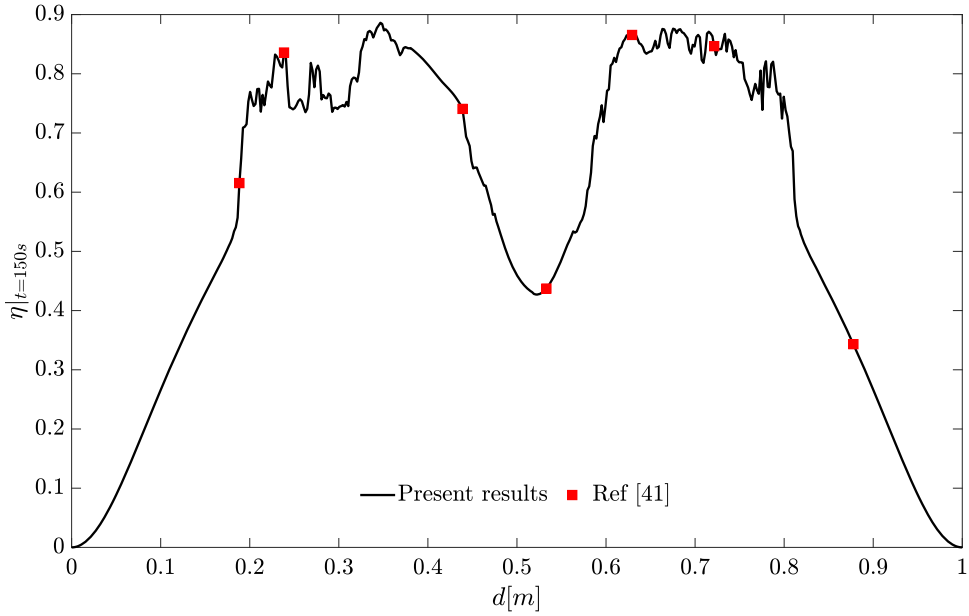

Fig. 18 Effect of NES position on input energy captured and dissipated – present results vs. Ref. [41]

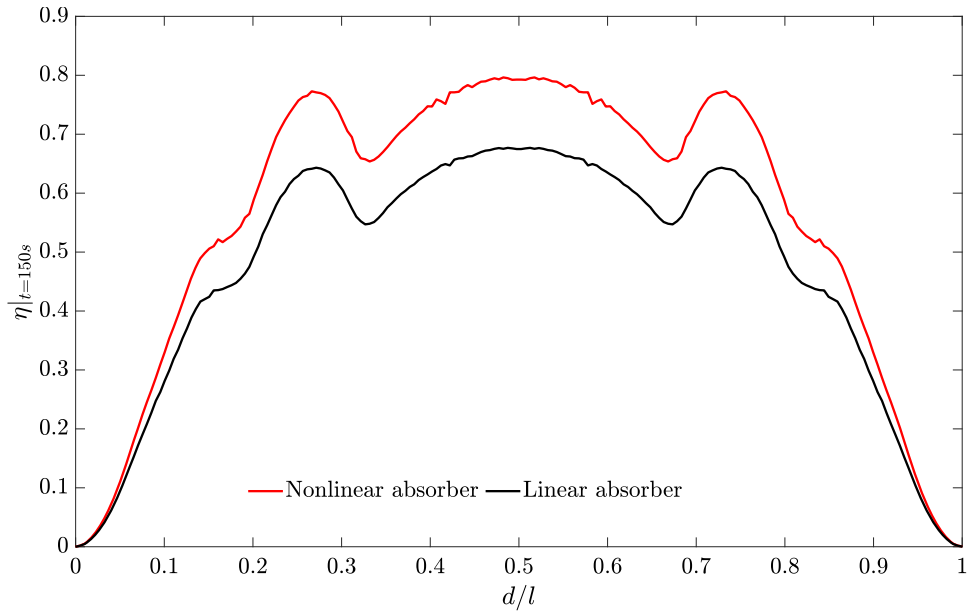

Fig. 19 Comparisons: effect of absorber position on the fraction of input energy captured and dissipated by linear and nonlinear absorbers

ings, wear-resistant guide rollers, and semi-active or hybrid designs that combine passive nonlinear components with low-power actuation. These developments could significantly improve durability, reduce maintenance demands, and increase the practical adoption of nonlinear moving absorbers in actual transmission-line networks.

4 Conclusion

In this study, we investigated the effectiveness of nonlinear moving vibration absorbers with different motion profiles in mitigating vibrations in overhead power-transmission lines, particularly near resonance at the first natural frequency. The equations of motion were obtained by applying Hamilton's principle, and the nonlinear aerodynamic lift force was represented using a nonlinear self-excited oscillator to capture wake-induced effects. We analyzed four motion profiles of nonlinear moving absorbers, including fixed, one-way, two-way, and two-two-way moving absorbers. We observed that in all cases, the nonlinear vibration absorber outperformed its linear counterpart in suppressing powerline vibrations.

A detailed parametric analysis was conducted to identify key system and design parameters and their optimal values to increase the effectiveness of the vibration absorber. We observed that higher absorber velocities offered better vibra-

tion suppression; however, excessive speeds could induce structural stress and diminish performance. We identified threshold values for nonlinear stiffness and damping, beyond which nonlinear moving vibration absorbers consistently outperformed their linear counterparts. Regarding mass distribution, we observed a lower span-mounted mass ratio reduced steady-state vibration amplitudes, although we also observed a trade-off between energy efficiency and vibration control, requiring careful tuning of system parameters. Furthermore, we observed that an increase in the damping and stall coefficients in the van der Pol oscillator led to lower vibration amplitudes, while higher values of the coupling coefficient amplified nonlinearities in the frequency response curves. The energy analysis also demonstrated that nonlinear absorbers, particularly those with two-two-way motion, were significantly more efficient in dissipating input energy than conventional fixed or linear absorbers.

Overall, this work presents a novel and comprehensive framework that jointly considers nonlinear wind excitation, nonlinear damping behavior, and dynamic absorber mobility. These findings offer practical design guidelines and demonstrate that nonlinear moving absorbers, when properly optimized, provide a robust and efficient solution for vibration mitigation in power transmission lines.

Author Contributions All authors contributed to the study's conception and design. E.B. performed material preparation, data collection, and analysis under the supervision of S.G. and O.B. For the manuscript, E.B. prepared the first draft, and all authors commented and revised on previous versions of the manuscript. All authors read and approved the final manuscript. O.B. received the funding to conduct this research.

Funding This work was funded by (CAREER) - ECCS #1944032: Towards a Self-Powered Autonomous Robot for Intelligent Power Lines Vibration Control and Monitoring.

Data Availability No datasets were generated or analysed during the current study.

Declarations

Conflict of interest No Conflict of interest are declared by the authors.

References

1. Doocy, E.S., Hard, A.R., Rawlins, C.B., Ikegami, R.: Transmission Line Reference Book: Wind-Induced Conductor Motion. Tech. rep, Gilbert/Commonwealth, Jackson, MI (USA) (1979)
2. Barry, O., Long, R., Oguamanam, D.C.D.: Simplified vibration model and analysis of a single-conductor transmission line with dampers. Proc. Inst. Mech. Eng. C J. Mech. Eng. Sci. **231**(22), 4150–4162 (2017)
3. Barry, O., Zu, J.W., Oguamanam, D.C.D.: Analytical and experimental investigation of overhead transmission line vibration. J. Vib. Control **21**(14), 2825–2837 (2015)
4. Migdalovici, M., Sireteanu, T., Videa, E.M.: Control of vibration of transmission lines. Int. J. Acoust. Vib. **15**(2), 65 (2010)
5. Mendonça, R., Caetano, E., Moutinho, C., Rodrigues, J., Saadi, O.: Characterisation of the damping performance of a stockbridge damper from laboratory tests of an overhead high-voltage transmission line conductor. In: Journal of Physics: Conference Series, Vol. 2647, IOP Publishing, p. 252027 (2024)
6. Malla, A.L., Gupta, S.K., Barry, O.: Nonlinear modeling and analysis of power lines with stockbridge dampers under vortex-induced vibrations. In: Dynamic Systems and Control Conference, Vol. 84287, American Society of Mechanical Engineers, p. V002T29A003 (2020)
7. Gupta, S.K., Malla, A.L., Barry, O.R.: Nonlinear vibration analysis of vortex-induced vibrations in overhead power lines with nonlinear vibration absorbers. Nonlinear Dyn. **103**, 27–47 (2021)
8. Casciati, F., Ubertini, F.: Nonlinear vibration of shallow cables with semiactive tuned mass damper. Nonlinear Dyn. **53**, 89–106 (2008)
9. Vaurigaud, B., Manevitch, L.I., Lamarque, C.-H.: Passive control of aeroelastic instability in a long span bridge model prone to coupled flutter using targeted energy transfer. J. Sound Vib. **330**(11), 2580–2595 (2011)
10. Basta, E., Ghommem, M., Emam, S.: Flutter control and mitigation of limit cycle oscillations in aircraft wings using distributed vibration absorbers. Nonlinear Dyn. **106**, 1975–2003 (2021)
11. Kakou, P., Bukhari, M., Wang, J., Barry, O.: On the vibration suppression of power lines using mobile damping robots. Eng. Struct. **239**, 112312 (2021)
12. Lu, M.L., Chan, J.K.: An efficient algorithm for aeolian vibration of single conductor with multiple dampers. IEEE Trans. Power Deliv. **22**(3), 1822–1829 (2007)
13. Barry, O., Zu, J.W., Oguamanam, D.C.D.: Nonlinear dynamics of stockbridge dampers. J. Dyn. Syst. Meas. Control. **137**(6), 061017 (2015)
14. Bukhari, M.A., Barry, O., Tanbour, E.: On the vibration analysis of power lines with moving dampers. J. Vib. Control **24**(18), 4096–4109 (2018)
15. Diana, G.: Modelling of Vibrations of Overhead Line Conductors: Assessment of the Technology. Springer, Berlin (2018)
16. Blevins, R.D.: Flow-Induced Vibration. New York (1977)
17. Khan, I., Shafie, S.: Rotating MHD flow of a generalized burgers' fluid over an oscillating plate embedded in a porous medium. Therm. Sci. **19**(suppl. 1), 183–190 (2015)
18. Khan, N.S., Islam, S., Gul, T., Khan, I., Khan, W., Ali, L.: Thin film flow of a second grade fluid in a porous medium past a stretching sheet with heat transfer. Alex. Eng. J. **57**(2), 1019–1031 (2018)
19. Zuhra, S., Khan, N.S., Khan, M.A., Islam, S., Khan, W., Bonyah, E.: Flow and heat transfer in water based liquid film fluids dispensed with graphene nanoparticles. Res. Phys. **8**, 1143–1157 (2018)
20. Srinil, N., Zanganeh, H.: Modelling of coupled cross-flow/in-line vortex-induced vibrations using double duffing and van der pol oscillators. Ocean Eng. **53**, 83–97 (2012)
21. Hartlen, R.T., Currie, I.G.: Lift-oscillator model of vortex-induced vibration. J .Eng. Mech. Div. **96**(5), 577–591 (1970)

22. Skop, R.A., Griffin, O.M.: On a theory for the vortex-excited oscillations of flexible cylindrical structures. J. Sound Vib. **41**(3), 263–274 (1975)
23. Basta, E., Gupta, S.K., Barry, O.: Frequency lock-in control and mitigation of nonlinear vortex-induced vibrations of an airfoil structure using a conserved-mass linear vibration absorber. Nonlinear Dyn. **112**, 1–21 (2024)
24. Iwan, W.D., Blevins, R.D.: A model for vortex induced oscillation of structures. J. Appl. Mech. **41**(3), 581–586 (1974)
25. Marra, A.M., Mannini, C., Bartoli, G.: Van der pol-type equation for modeling vortex-induced oscillations of bridge decks. J. Wind Eng. Ind. Aerodyn. **99**(6–7), 776–785 (2011)
26. Pust, L., Pesek, L.: Blades forced vibration under aero-elastic excitation modeled by van der pol. Int. J. Bifurcat. Chaos **27**(11), 1750166 (2017)
27. Main, J.A., Jones, N.P.: Free vibrations of taut cable with attached damper. i i: Nonlinear damper. J. Eng. Mech. **128**(10), 1072–1081 (2002)
28. Basta, E., Ghommem, M., Emam, S.: Vibration suppression of nonlinear rotating metamaterial beams. Nonlinear Dyn. **101**, 311–332 (2020)
29. Pazooki, A., Goodarzi, A., Khajepour, A., Soltani, A., Porlier, C.: A novel approach for the design and analysis of nonlinear dampers for automotive suspensions. J. Vib. Control **24**(14), 3132–3147 (2018)
30. Li, H., Zhang, P., Song, G., Patil, D., Mo, Y.: Robustness study of the pounding tuned mass damper for vibration control of subsea jumpers. Smart Mater. Struct. **24**(9), 095001 (2015)
31. Samani, F.S., Pellicano, F.: Vibration reduction on beams subjected to moving loads using linear and nonlinear dynamic absorbers. J. Sound Vib. **325**(4–5), 742–754 (2009)
32. Zhang, Y., Kong, X., Yue, C., Guo, J.: Characteristic analysis and design of nonlinear energy sink with cubic damping considering frequency detuning. Nonlinear Dyn. **111**(17), 15817–15836 (2023)
33. Xu, K.-F., Zhang, Y.-W., Zang, J., Niu, M.-Q., Chen, L.-Q.: Integration of vibration control and energy harvesting for whole-spacecraft: experiments and theory. Mech. Syst. Signal Process. **161**, 107956 (2021)
34. Xu, K.-F., Niu, M.-Q., Zhang, Y.-W., Meng, C.-Y., Chen, L.-Q.: A nonlinear energy sink enhanced by active varying stiffness for spacecraft structure: theory, simulation, and experiment. Mech. Syst. Signal Process. **204**, 110787 (2023)
35. Xu, K., Niu, M., Zhang, Y., Chen, L.: An active high-static-low-dynamic-stiffness vibration isolator with adjustable buckling beams: theory and experiment. Appl. Math. Mech. **45**(3), 425–440 (2024)
36. Barry, O.R., Tanbour, E.Y., Vaja, N.K., Tanbour, H.: Asymmetric aeolian vibration damper, US Patent 9948081 (17 Apr 2018)
37. Daqaq, M.F.: Dynamics of Particles and Rigid Bodies: A Self-learning Approach. John Wiley & Sons, New Jersey (2018)
38. Skop, R.A., Balasubramanian, S.: A new twist on an old model for vortex-excited vibrations. J. Fluids Struct. **11**(4), 395–412 (1997)
39. Barry, O., Zu, J.W., Oguamanam, D.C.D.: Forced vibration of overhead transmission line: analytical and experimental investigation. J. Vib. Acoust. **136**(4), 041012 (2014)
40. Soares, R.M., del Prado, Z.J., Gonçalves, P.B.: On the vibration control of beams using a moving absorber and subjected to moving loads. Mech. Comput. **29**(17), 1829–1840 (2010)
41. Georgiades, F., Vakakis, A.F.: Dynamics of a linear beam with an attached local nonlinear energy sink. Commun. Nonlinear Sci. Numer. Simul. **12**(5), 643–651 (2007)